*Geophys. J. Int.* (2006) **166,** 67–75 doi: 10.1111/j.1365-246X.2006.02959.x





# CHAOS—a model of the Earth's magnetic field derived from CHAMP, Ørsted, and SAC-C magnetic satellite data

Nils Olsen,[1] Hermann Lühr,[2] Terence J. Sabaka,[3] Mioara Mandea,[2] Martin Rother,[2] Lars Tøffner-Clausen[1] and Sungchan Choi[2]

[1] *Danish National Space Center, Juliane Maries Vej* 30, 2100 *Copenhagen, Denmark. E-mail: nio@spacecenter.dk*
[2] *GeoForschungsZentrum Potsdam,* 14473 *Potsdam, Germany*
[3] *Geodynamics Branch, NASA GSFC, Greenbelt, MD, USA*

Accepted 2006 February 14. Received 2006 February 14; in original form 2005 December 9

## SUMMARY

We have derived a model of the near-Earth magnetic field (up to spherical harmonic degree $n = 50$ for the static field, and up to $n = 18$ for the first time derivative) using more than 6.5 yr of high-precision geomagnetic measurements from the three satellites Ørsted, CHAMP and SAC-C taken between 1999 March and 2005 December.

Our modelling approach goes in several aspects beyond that used for recent models: (i) we use different data selection criteria and allow for higher geomagnetic activity (index $Kp \leq 2o$), thus we include more data than previous models; (ii) we describe the temporal variation of the core field by splines (for $n \leq 14$); (iii) we take magnetometer vector data in the instrument frame and co-estimate the Euler angles that describe the transformation from the magnetometer frame to the star imager frame, avoiding the inconsistency of using vector data that have been aligned using a different (pre-existing) field model; (iv) we account for the bending of the CHAMP optical bench connecting magnetometer and star imager by estimating Euler angles in 10 day segments and (v) we co-estimate degree-1 external fields separately for every 12 hr interval.

The model provides a reliable representation of the static (core and crustal) field up to spherical harmonic degree $n = 40$, and of the first time derivative up to $n = 15$.

**Key words:** Earth's magnetic field, geomagnetic secular variation, geomagnetism, lithosphere, satellite, spherical harmonics.

## 1 INTRODUCTION

The beginning of the *International Decade of Geopotential Research* that has been declared by the *International Union of Geophysics and Geodesy* was marked by the launch of the Ørsted satellite in 1999 February. Ørsted was followed by the CHAMP satellite and the SAC-C satellite with the Ørsted-2 experiment, launched in 2000 July and November, respectively. All three missions carry essentially the same instrumentation and provide magnetic field observations from space with unprecedented accuracy. Due to the somewhat different altitudes (Ørsted: 630–860 km, CHAMP: 350–450 km; SAC-C: 700 km) and drift rates through local time, the spacecrafts sense the various internal and external field contributions differently.

During the first years of the *Decade*, various geomagnetic field models of increasing complexity and accuracy have been derived. One of the first models, the *Ørsted Initial Field Model* (Olsen *et al.* 2000), represents a snapshot of the magnetic field at epoch 2000.0 up to spherical harmonic degree $n = 19$ and was estimated from a few weeks of Ørsted data around 2000 January 1. Using 14 months of Ørsted data and applying classical selection criteria based on local time and geomagnetic activity, Langlais *et al.* (2003) computed a 29-degree internal field model and a 13-degree model of linear secular variation for the period 1999–2000.

A model based on more than 2 yr (1999 March to 2001 September) of Ørsted data was derived by Olsen (2002). This model is a spherical harmonic expansion of the static field ($n \leq 29$) and of the linear secular variation ($n \leq 13$) for epoch 2000.0 based on Ørsted data applying new modelling approaches for a correct statistical treatment of data errors and for considering external field contributions. Large-scale magnetospheric contributions were estimated up to degree 2; the zonal coefficients of which vary with annual and semi-annual periodicity, and degree-1 coefficients were modulated with the strength of the magnetospheric ring-current as measured simultaneously by globally distributed geomagnetic observatories. The same model parametrization was chosen for the CO2 model (Holme *et al.* 2003); however, CHAMP vector and scalar and SAC-C scalar data had been used in addition to the Ørsted data.

More recently, a new model line (POMME: POtsdam Magnetic Model of the Earth) was introduced (Maus *et al.* 2005), parametrizing magnetospheric sources in their intrinsic coordinate systems

(i.e. solar magnetospheric (SM) coordinates for describing near magnetospheric currents like the ring-current, and geocentric solar magnetospheric (GSM) for describing far magnetospheric current systems like the tail currents (see Kivelson & Russell 1995 for a definition of SM and GSM). This treatment and the co-estimation of a time-varying correction of the $D_{st}$-index that is used to parametrize the ring-current (Lesur *et al.* 2005; Olsen *et al.* 2005), leads to a more accurate determination especially of the secular variation.

In addition to these models describing core and low-degree lithospheric fields, specific models of the lithospheric field alone have been derived mainly using CHAMP vector data, after removal of external field contributions by along-track data filtering on an orbit-by-orbit basis. The latest version of that model series, called *MF4* (Maus *et al.* 2006), describes the lithospheric field up to degree $n = 90$; however, coefficients with $n \geq 60$ are damped.

Ørsted (vector and scalar) and CHAMP (scalar) observations have also been used, together with data from the POGO and Magsat satellites and ground based observations, in the latest version of the *comprehensive model*, *CM4* (Sabaka *et al.* 2004). This model attempts to describe the major quiet-time contributions to the Earth's magnetic field (core and crustal fields, fields due to ionospheric and large-scale magnetospheric currents, and due to secondary, Earth-induced, currents) by co-estimation of all these sources.

The present paper describes a new model, one goal of which is to describe the static (core and crustal) field (up to about degree $n = 50$). Special emphasis is, however, put on an accurate determination of the temporal changes during the 6.5 yr interval. Recognizing the unpredictability and chaotic nature of the Earth's magnetic field, we call our model *CHAOS*, the *CHAMP*, Ørsted and SAC-C model of Earth's magnetic field.

To obtain the described goals based on satellite data only, we used an approach that goes in several aspects beyond that applied to previous modelling efforts:

(i) Our data selection criteria differ from that used for previous models: at non-polar latitudes we allow for higher geomagnetic activity (up to $Kp = 2o$) than most recent models, thus we have include more data. Polar latitude data are selected according to the strength of the 'merging electric field' $E_m$ (Kan & Lee 1979) and illumination conditions.

(ii) The availability of more than 6.5 yr of high-precision satellite data provides a unique opportunity for studying the fine structure of secular variation. However, secular variation can no longer be regarded linear if a time span of several years is considered. The inclusion of higher (quadratic, cubic, . . .) temporal terms may lead, however, to unwanted behaviours near the edges of the time interval. We, therefore, describe the time change of the low-degree ($n \leq 14$) coefficients by cubic B-splines, a technique that has not been done previously for models that are based solely on satellite data.

(iii) Accurate orientation of the magnetic field vector measured on a satellite is a demanding task. For the mediation of this problem we co-estimate the Euler angles connecting the attitude determination system (star imager) with the vector magnetometer. Therefore, we use the vector data in the instrument frame rather than data that were aligned using a pre-existing field model.

(iv) This in-flight alignment of the vector data is particularly important for the CHAMP measurements due to thermomechanical bending of the CHAMP optical bench that connects vector magnetometer and star imager. We account for this variation by estimating time-dependent Euler angles. In addition, a flaw in the star-imager onboard software has recently been detected. An algorithm correcting the CHAMP attitude data for this effect has been applied. For the present model we use these new attitude data.

(v) Finally, we co-estimated a residual $n = 1$ external field contribution in dipole coordinates for each 12 hr interval. This describes a large-scale external field that is not covered by the $D_{st}$-index, and may be interpreted as correcting any error of the $D_{st}$ baseline.

## 2 DATA SELECTION AND PRE-PROCESSING

We use Ørsted scalar and vector data between 1999 March and 2005 December, CHAMP scalar and vector data between 2000 August and 2005 December (vector data only after 2001 January), and SAC-C scalar data between 2001 January and 2004 December. All data are selected according to quiet geomagnetic conditions as defined by the following criteria. First, at all latitudes we require that the $D_{st}$-index does not changed by more than 2 nT h$^{-1}$. At non-polar latitudes (equatorwards of 60° dipole latitude) $Kp \leq 2o$ has to be fulfilled. ($Kp \leq 2o$ corresponds to a variation (peak-to-peak) range of $\leq 7$ nT, a value that is compatible with the model misfit, *cf.* Table 1). For regions polewards of 60° we require that the merging electric field, $E_m$, at the magnetopause (Kan & Lee 1979) is less than 0.8 mV m$^{-1}$. This threshold value was suggested by Ritter *et al.* (2004) based on their analysis of quiet-time CHAMP polar passes. For the years considered here (1999–2005), 43 per cent of the data have $E_m < 0.8$ mV m$^{-1}$, 48 per cent have $Kp \leq 2o$, 76 per cent have $dD_{st}/dt < 2$ nT h$^{-1}$, and 38 per cent have both $Kp \leq 2o$ and $dD_{st}/dt < 2$ nT h$^{-1}$ fulfilled. Only data from dark regions (sun 10° below horizon) were used, to reduce contributions from ionospheric currents. Vector data have been taken for dipole latitudes equatorwards of ±60°, to avoid the disturbing effect of field-aligned currents, which only influence the vector components but not field intensity. During the geomagnetic quiet periods considered here, these currents do not occur at latitudes equatorwards of 60° (Feldstein & Starkov 1970). Scalar data were used for regions polewards of ±60° or if attitude data were not available. Only non polar CHAMP data after local midnight are used, to avoid the influence of the diamagnetic effect of dense plasmas (Lühr *et al.* 2003). Due to their higher altitudes, a corresponding rejection of pre-midnight data is not necessary for Ørsted and SAC-C.

We also tried different values for the above described selection criteria (for instance allowing for a larger value of $dD_{st}/dt$). However, from the limited amount of experiments that we performed we concluded that the above described data selection criteria lead to the 'best' field model, for example, concerning the noise level as seen in

**Table 1**. Number $N$ of data points, mean, and rms misfit (in nT) of the model.

| | component | $N$ | mean | rms |
|---|---|---|---|---|
| all | $F_{\text{polar}}$ | 155,717 | −0.10 | 4.80 |
| | $F_{\text{nonpolar}} + B_B$ | 529,444 | 0.03 | 2.60 |
| Ørsted | $F_{\text{polar}}$ | 64,396 | 0.53 | 4.35 |
| | $F_{\text{nonpolar}} + B_B$ | 259,290 | 0.29 | 2.47 |
| | $B_\perp$ | 146,556 | 0.06 | 7.74 |
| | $B_3$ | 146,556 | 0.02 | 3.56 |
| CHAMP | $F_{\text{polar}}$ | 55,574 | −0.97 | 5.85 |
| | $F_{\text{nonpolar}} + B_B$ | 124,749 | −0.33 | 2.79 |
| | $B_\perp$ | 115,129 | 0.00 | 3.55 |
| | $B_3$ | 115,129 | 0.03 | 3.31 |
| SAC-C | $F_{\text{polar}}$ | 35,745 | −0.06 | 3.99 |
| | $F_{\text{nonpolar}}$ | 145,405 | −0.14 | 2.65 |

the Mauersberger-Lowes power spectrum, or when comparing with other models.

Data sampling interval is 60 s; weights proportional to $\sin\theta$ (where $\theta$ is geographic colatitude) are applied to simulate an equal-area distribution. Ørsted vector data show anisotropic errors due to attitude uncertainty when calculating the orientation from the single star camera (Olsen *et al.* 2000); such an anisotropy is also present in the CHAMP data from dawn–dusk orbits when one of the two cameras is sun blinded. This behaviour is explicitly considered in the inversion (Holme & Bloxham 1996; Holme 2000).

Traditionally, geomagnetic field modelling is done using vector data that are both calibrated and aligned. Data *calibration*, the conversion of the raw vector magnetometer readings into scaled magnetic field components (in units of nT) in the orthogonal coordinate system of the sensor, is done by comparing the output of the *Vector Fluxgate Magnetometer (VFM)* with the magnetic field intensity measurements obtained simultaneously with an absolute scalar Overhauser magnetometer. Thus the calibration is performed for each satellite separately (*cf.* Olsen *et al.* 2003 for more information on the calibration issue).

Merging these vector data with attitude data and transforming them to $(B_r, B_\theta, B_\phi)$ (i.e. the upward, northward and eastward component) requires, however, one additional calibration step, called data *alignment*, which is the precise determination of the transfer angles (Euler angles) between the star imager and the vector magnetometer. This requires models of the star constellation, and of the ambient magnetic field. The former model is known with high precision (e.g. Hipparcos catalogue, *ESA*, 1997). The limiting factor for the alignment is the accuracy of the ambient magnetic field *to be known at the time and position of each data point*. It is the purpose of this exercise to obtain an improved magnetic field model. To avoid the inconsistency of deriving a field model from vector data that have been aligned using a different (pre-existing) magnetic field model, we do the data alignment as part of the modelling effort.

## 3 MODEL PARAMETRIZATION

The model consists of two parts: spherical harmonic expansion coefficients describing the magnetic field vector in the local north, east, centre (*NEC*) coordinate system, and sets of Euler angles needed to rotate the vector readings from the magnetometer frame to the star imager frame (and finally, after merging with the attitude data, to the *NEC* frame).

As mentioned before, we assume that the magnetic field in the *NEC* system,

$$\mathbf{B}_{\mathrm{NEC}} = \begin{pmatrix} B_{\mathrm{North}} \\ B_{\mathrm{East}} \\ B_{\mathrm{Center}} \end{pmatrix} = \begin{pmatrix} -B_\theta \\ +B_\phi \\ -B_r \end{pmatrix} = -\mathrm{grad}\, V, \tag{1}$$

can be derived from a magnetic scalar potential $V = V^{\mathrm{int}} + V^{\mathrm{ext}}$ consisting of a part, $V^{\mathrm{int}}$, describing internal sources, and a part, $V^{\mathrm{ext}}$, describing external sources (including their Earth-induced counterparts). Both are expanded in terms of spherical harmonics.

For the internal part this yields

$$V^{\mathrm{int}} = a \sum_{n=1}^{N_{\mathrm{int}}} \sum_{m=0}^{n} \left(g_n^m \cos m\phi + h_n^m \sin m\phi\right) \left(\frac{a}{r}\right)^{n+1} P_n^m(\cos\theta), \tag{2}$$

where $a = 6371.2$ km is a reference radius, $(r, \theta, \phi)$ are geographic coordinates, $P_n^m$ are the associated Schmidt semi-normalized Legendre functions, $\{g_n^m, h_n^m\}$ are the Gauss coefficients describing internal sources, and $N_{\mathrm{int}}$ is the maximum degree and order of the internal expansion, which is taken here to $N_{\mathrm{int}} = 50$.

The time dependence of the internal Gauss coefficients $\{g_n^m(t), h_n^m(t)\}$ is for $n \le 14$ described by cubic B-splines (Schumaker 1981; De Boor 2001; Bloxham & Jackson 1992) with a 1-yr knot separation and four-fold knots at the endpoints, $t = 1999.0$ and $t = 2006.0$. This yields six interior knots (at 2000.0, 2001.0, ..., 2005.0) and four exterior knots at each endpoint, 1999.0 and 2006.0, resulting in 10 basic B-spline functions, $M_l(t)$, shown in Fig. 1. Although higher degree terms are expected to have shorter timescales compared to lower degrees, we do not use a spline representation for coefficients above degree $n = 14$ since the present data probably do not allow for resolving their short-period time variation. Coefficients with degree $n > 14$ are, therefore, assumed to vary linearly in time for $n = 15$–$18$, and to be static for $n = 19$–$50$. Thus the temporal behaviour of each Gauss coefficient is described by

$$\begin{aligned} g_n^m(t) &= \textstyle\sum_{l=1}^{10} g_{n,l}^m \cdot M_l(t) && \text{for } n = 1-14 \\ &= g_n^m(t_0) + (t - t_0) \cdot \dot{g}_n^m(t_0) && \text{for } n = 15-18, \\ &= g_n^m(t_0) && \text{for } n = 19-50 \end{aligned} \tag{3}$$

and similar for $h_n^m$. This gives in total 4752 internal Gauss coefficients.

The external potential, $V^{\mathrm{ext}}$, describes large-scale magnetospheric sources and is expanded according to

$$\begin{aligned} V^{\mathrm{ext}} = {} & a \sum_{n=1}^{2} \sum_{m=0}^{n} \left(q_n^m \cos m T_d + s_n^m \sin m T_d\right) P_n^m(\cos\theta_d) \\ & + a \sum_{m=0}^{1} \left(\hat{q}_1^m \cos T_d + \hat{s}_1^m \sin T_d\right) \\ & \cdot \left\{ E_{\mathrm{st}}(t) \left(\frac{r}{a}\right) + I_{\mathrm{st}}(t) \left(\frac{a}{r}\right)^2 \right\} P_1^m(\cos\theta_d) \\ & + a \sum_{n=1}^{2} q_n^{0,\mathrm{GSM}} R_n^0(r, \theta, \phi). \end{aligned} \tag{4}$$

The first three lines of this equation represent an expansion in the *SM* coordinate system and describe mainly contributions from the near magnetosphere (e.g. the magnetospheric ring current); the expansion in *GSM* coordinates used in the last line of the equation aims at describing contributions from far magnetospheric current systems (e.g. tail currents). $\theta_d$ and $T_d$ are dipole colatitude and dipole local time, respectively (which are identical to colatitude and longitude in the *solar magnetic* coordinates system), and $E_{\mathrm{st}}$, $I_{\mathrm{st}}$ are time series of the decomposition of the $D_{\mathrm{st}}$-index, $D_{\mathrm{st}}(t) = E_{\mathrm{st}}(t) + I_{\mathrm{st}}(t)$, into external and induced parts, respectively (Maus & Weidelt 2004; Olsen *et al.* 2005). The functions $R_n^0$ are modifications of the Legendre functions to account explicitly for induced field contributions due to the wobble of the GSM $z$-axis with respect to the Earth's rotation axis. For a non-conducting Earth these functions would be $R_n^0 = (\frac{r}{a})^n P_n^0(\cos\theta_{\mathrm{GSM}})$ where $\theta_{\mathrm{GSM}}$ is colatitude in the GSM coordinate system; considering a plausible 1D model of mantle conductivity leads to a representation of $R_n^0$ similar to the expansion outlined in Maus & Lühr (2005).

In addition, large-scale magnetospheric fields that are not described by the above expansion are considered by solving for time-varying degree-1 coefficients $q_1^0, q_1^1, s_1^1$. This is especially important for the coefficient $q_1^0$, which can be interpreted as a baseline uncertainty in the $D_{\mathrm{st}}$-index. We, therefore, solve for $q_1^0$ in bins of 12 hr length, whereas the equatorial dipole coefficients $q_1^1, s_1^1$ are solved for in bins of 5 day length. We only solve for coefficients if there are

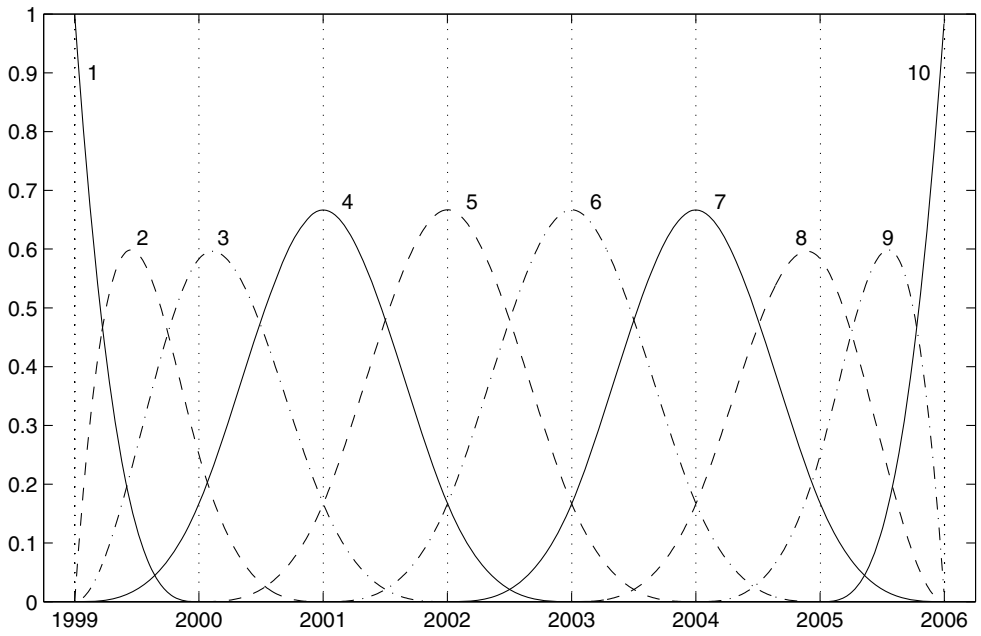


**Figure 1.** Schematic of the cubic B-spline basic functions, $M_l(t)$, $l = 1$–10, used to represent the time change of each Gauss coefficient of degree $n \leq 14$. There are six interior knots and four exterior knots at each endpoint.

at least 50 data points in the corresponding bin; otherwise data of that bin are discarded. This gives a total of 3754 external coefficients.

As mentioned before, we also solve, in addition to the spherical harmonic coefficients of eqs (2)–(4), for the Euler angles of the rotation between the coordinate systems of the *vector fluxgate magnetometer (VFM)* and of the *star imager (STR)*. Since a rotation does not change the length of a vector, magnetic field intensity is not affected by this rotation, which means that only vector data are sensitive to the Euler angles. Let $\underline{\underline{\mathbf{R}}}_3$ be the matrix which rotates the magnetic field $\mathbf{B}_{\rm NEC}$ from the *NEC* system to the magnetic field $\mathbf{B}_{\rm ICRF} = \underline{\underline{\mathbf{R}}}_3 \cdot \mathbf{B}_{\rm NEC}$ in the *International Celestial Reference Frame* (ICRF); $\underline{\underline{\mathbf{R}}}_3$ is derived from satellite position and time (Seeber 2004). Next, $\underline{\underline{\mathbf{R}}}_2$ is a matrix which rotates the magnetic field $\mathbf{B}_{\rm STR} = \underline{\underline{\mathbf{R}}}_2 \cdot \mathbf{B}_{\rm ICRF}$ from the *ICRF* frame to the star imager *STR* frame and is constructed from the attitude data measured by the star imager. Finally, $\underline{\underline{\mathbf{R}}}_1$ is the matrix which rotates from the *STR* coordinate system to the orthogonal magnetometer (*VFM*) coordinate system; this rotation is described by the three Euler angles that we co-estimate.

Due to thermomechanical instabilities of the magnetometer/star-imager system, the CHAMP Euler angles vary with time; we account for this variation by estimating separate sets of Euler angles for each 10 day data segment. There is no indication for a mechanical instability of the Ørsted magnetometer/star imager assembly and, therefore, we assume that the Ørsted Euler angles are time independent. However, to account for a star-imager software update on 2000 January 24, which resulted in a change of the optical axis of the instrument, we estimate two sets of Ørsted Euler angles, one for the time before and one for the time after 2000 January 24. This yields 119 sets of Euler angles (2 for Ørsted, and 117 for CHAMP), that is, 357 additional model parameters, resulting in 8863 model parameters in total. Although the goal of our *CHAOS* model is a precise description of the internal magnetic field, 46 per cent of the model parameters (4111 of 8863 parameters) describe non-internal (external field and payload system) parameters. The co-estimation of these additional parameters is done entirely to secure an optimal description of the internal field. As in the case of our data selection criteria, we also tried various other parametrisations of the external fields (for instance bin sizes of 24 and 48 hr for the magnetospheric coefficient $q_1^0$) but found that the chosen values resulted in the best internal field model.

To summarize: the relationship between the magnetic vector in the magnetometer coordinate system, $\mathbf{B}_{\rm VFM}$, and the magnetic potential $V$ in the local *NEC* coordinate system is given by

$$\mathbf{B}_{\rm VFM} = \underline{\underline{\mathbf{R}}}_1 \cdot \underline{\underline{\mathbf{R}}}_2 \cdot \underline{\underline{\mathbf{R}}}_3 \cdot \mathbf{B}_{\rm NEC} = -\underline{\underline{\mathbf{R}}}_1 \cdot \underline{\underline{\mathbf{R}}}_2 \cdot \underline{\underline{\mathbf{R}}}_3 \cdot \text{grad}\, V. \quad (5)$$

This equation connects the data (the magnetic field observations $\mathbf{B}_{\rm VFM}$ in the magnetometer frame, collected in the data vector $\mathbf{d}_{\rm obs}$) with the model parameters (the spherical harmonic expansion coefficients of the scalar potential $V$ of eqs (2)–(4) and the sets of Euler angles describing $\underline{\underline{\mathbf{R}}}_1$, collected together in the model vector $\mathbf{m}$).

## 4 MODEL ESTIMATION

We minimize the sum of the squared differences between the observed magnetic field in the instrument frame, $\mathbf{B}_{\rm VFM}^{\rm obs}$, and the model predictions of eq. (5). This means that we do the model estimation in the magnetometer frame, contrary to previous models, which used vector data in the *NEC* frame and thus minimize the squared differences between the observations, $\mathbf{B}_{\rm NEC}^{\rm obs}$ and the model predictions of eq. (1).

Since we also use scalar data, and due to the co-estimation of the alignment parameters (Euler angles), the estimation of the model parameters is a non-linear problem and has to be solved iteratively. We use an *iteratively reweighted least-squares approach*, minimizing the chi-squared misfit

$$\chi^2 = \mathbf{e}^T \underline{\underline{C}}^{-1} \mathbf{e} + \lambda \mathbf{m}^T \underline{\underline{\Lambda}} \mathbf{m}, \quad (6)$$

where $\mathbf{m}$ is the model vector and the residuals vector $\mathbf{e} = \mathbf{d}_{\rm obs} - \mathbf{d}_{\rm mod}$ is the difference between observation $\mathbf{d}_{\rm obs}$ and model prediction $\mathbf{d}_{\rm mod}$. The data covariance matrix $\underline{\underline{C}}$ contains the data errors multiplied by Huber weights (to account for the non-Gaussian distribution of the data residuals); its non-diagonal elements accounts

for the anisotropic errors due to attitude noise (see Olsen 2002 for details). $\underline{\underline{\Lambda}}$ is a block diagonal damping matrix, which constrains the second and higher order time derivatives of the core field. Only elements corresponding to the spline coefficients of the first line of eq. (3) are non-zero; they are given by

$$\frac{(n+1)}{\Delta t}\int_{t=1999}^{2006}\frac{d^2M_l(t)}{dt^2}\frac{d^2M_k(t)}{dt^2}dt, \tag{7}$$

with $\Delta t = 2006 - 1999 = 7$ yr, which minimizes the mean square magnitude of the second time derivative of **B**, integrated over the Earth's surface and averaged over time:

$$\langle\ddot{\mathbf{B}}^2\rangle = \frac{1}{\Delta t}\int_{t=1999}^{2006}\int\left|\frac{\partial^2\mathbf{B}}{\partial t^2}\right|^2 d\Omega\, dt = \mathbf{m}^T\underline{\underline{\Lambda}}\mathbf{m}. \tag{8}$$

The parameter $\lambda$ controls the strength of this damping; $\lambda = 0$ corresponds to an undamped model; the chosen value, $\lambda = 1\cdot 10^4$ $(\mathrm{nT\,yr^{-2}})^{-2}$, was found to be a good compromise between data misfit and model smoothness, and results in a mean squared value $\langle\ddot{\mathbf{B}}^2\rangle = 19\,(\mathrm{nT\,yr^{-2}})^2$. Note that this damping neither directly affects the static field nor the first time derivative, which are left undamped.

## 5 RESULTS AND DISCUSSION

Number of data points, residual means and root-mean-squared (rms) values of the model are listed in Table 1. The mean values (data minus model) are close to zero and do not exceed 0.3 nT at non-polar latitudes, confirming the validity of the magnetometer calibrations of the three satellites. The biases at polar latitudes are larger and exhibit even different signs for the three missions (Ørsted: +0.53 nT; CHAMP: −0.97 nT; SAC-C: −0.06 nT). These values cannot be regarded as a measure of the data quality, but reflect only how well the model fits the observations at latitudes where contributions from polar ionospheric current systems are rather important. The scalar rms misfit is between 2.47 nT (Ørsted), 2.65 nT (SAC-C) and 2.79 nT (CHAMP) at non-polar latitudes, and between 4.0 nT and 5.85 nT at polar latitudes. The higher values compared to non-polar latitudes could indicate unmodelled contributions from polar ionospheric current systems; the higher value for CHAMP, compared to Ørsted and SAC-C, is probably caused by the lower altitude, which brings CHAMP closer to ionospheric sources. Statistics for the vector components are given in a coordinate system that is defined by the bore-sight of the star imager and the ambient field direction (*cf.* Olsen *et al.* (2000) for details). The two components $B_\perp$ and $B_3$ are both perpendicular to the main field. Attitude noise if only data from one star imager head are available (which is always the case for Ørsted, and happens when CHAMP is in a dawn–dusk orbit) affects mostly $B_\perp$. Consequently, the rms misfit of $B_\perp$ is 7.74 nT for Ørsted, but less than half that value for CHAMP (3.55 nT). The rms misfit of the third vector component, $B_3$, is similar for Ørsted (3.56 nT) and CHAMP (3.31 nT). All these values indicate an excellent consistency of the data from the three different satellites, and a remarkable agreement with the obtained magnetic field model.

Fig. 2 shows Mauersberger-Lowes spectra of the first and second time derivatives of various models. Such a power spectrum provides information about the accuracy of a given model as a function of spherical harmonic degree, for instance about its level of noise. The spectrum of the first time derivative as obtained from 6 months of Magsat satellite data and from 91 observatories is shown in black (Langel & Estes 1985). Only coefficients up to $n = 6$ are above the noise level, indicated by the flat part of the spectrum at about 70 $(\mathrm{nT\,yr^{-1}})^2$. Additional use of data from the DE-2 satellite between 1981 September and 1983 January improves the secular variation determination slightly and reduces the noise level to about 30 $(\mathrm{nT\,yr^{-1}})^2$ (magenta curve, Langel *et al.* (1988)). A major improvement was possible by an analysis of the first 2 yr of Ørsted observations, which reduces the noise level to about 1 $(\mathrm{nT\,yr^{-1}})^2$ (blue curve, Olsen 2002); first time derivative coefficients up to $n = 11$ are resolved. Yet another order of magnitude in noise reduction was obtained by Maus *et al.* (2005) in their combined analysis of Ørsted and CHAMP data spanning more than 5 yr (green curve), resulting in a determination of the first time derivative up to $n = 13$. (Note that coefficients of the first time derivative of all models presented in this figure are undamped; however, those of the final model (not shown here) of Maus *et al.* (2005) are damped for $n > 13$). Finally, the first time derivative of the model presented in this paper has a noise level as low as 0.02 $(\mathrm{nT\,yr^{-1}})^2$, which allows its determination up to $n = 15$ (the presented spectrum is calculated from the spline representation for epoch $t = 2002.5$).

In addition to the first time derivative, Maus *et al.* (2005) also estimated the second time derivative, the spectrum of which is also

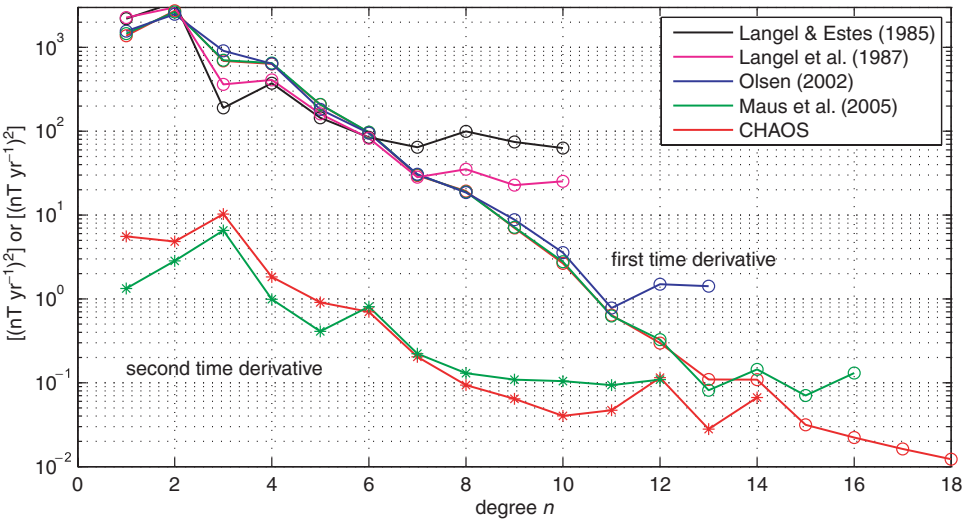


**Figure 2.** Lowes-Mauersberger spectra of first and second time derivatives for various magnetic field models.

shown in the figure, together with that of our new model. Note that this part of our model is damped.

Probably the most significant improvement of the presented model compared to previous models is its ability to map small-scale structure of the secular variation. The crustal field exceeds the core field for spherical harmonic degrees above $n = 13$ and it is, therefore, not possible to infer small-scale structures of the (static) core field. However, since the lithospheric field is time independent (at least on the timescales considered here), the *time changes* of the core field are, in principle, observable at all spatial wavelengths. As shown in Fig. 2, determination of time variation was previously restricted to degrees $n \leq 13$. Our new model resolves first time derivative coefficients beyond $n = 13$, which means that it is for the first time possible to infer the time change (secular variation) of the core field down to smaller scales (1400 km length at the core-mantle boundary) than the (static) core field itself.

Although a detailed interpretation of the core field part of our model is beyond the scope of this paper, we want to point out some implications that it may have on geodynamo modelling. It is generally accepted that the higher spherical harmonic degrees of the secular variation are related to processes with shorter timescales. Stacey (1992) defined a characteristic timescale

$$\tau(n) = \sqrt{\frac{\sum_m \left(g_n^m\right)^2 + \left(h_n^m\right)^2}{\sum_m \left(\dot{g}_n^m\right)^2 + \left(\dot{h}_n^m\right)^2}}, \tag{9}$$

which he denoted as *reorganization time* since it is 'related to the electromagnetic relaxation times of current loops in the core that would produce the different harmonic features of the field'. Hulot & Le Mouël (1994) use the same definition but call $\tau$ the *typical correlation time*, with $\tau(n) = 1/\sqrt{R(n)}$, where $R(n)$ is the degree-ratio of the power in the first time derivative to that of the static field (Holme & Olsen 2006). The red circles of Fig. 3 present the dependence of $\tau$ on spherical harmonic degree $n$ (i.e. spatial length scale) calculated from our model coefficients applied to eq. (9). Holme & Olsen (2006) show that a power law model, $R = An^B$ (corresponding to $\tau = A^{-1/2}n^{-B/2}$), gives a better representation than an exponential fit $R = Ae^{Bn}$. The black curve in the figure is the power law expression $\tau = 890\ n^{-1.35}$ yr, obtained by fitting the function to the observed values within the range $n = 1$ and $n = 13$. Due to the dominance of the crustal field at smaller scales, no reliable coefficients for the core field are available for degrees $n > 13$, We can, however, extrapolate the power fit up to degree 16 (the resolution of our secular variation). Here we obtain a re-organization time, $\tau = 20$ yr, which is close to the period where dissipation effects start to be important for the geodynamo.

Also, the lithospheric part ($n \leq 40$) of our new model is superior to previous models. Indications for this are given in the Figs 4–6. The left panel of Fig. 4 shows the static field spectrum of various models, and the spectra of the differences between these models. The integrated power (degrees $n = 16$–$40$) of our new model (black curve) is 5 per cent below that of model *CM4* of Sabaka *et al.* (2004) (light green), but 25 per cent above that of model *MF4* of Maus *et al.* (2006) (magenta). The smallest difference is found between our model and *CM4* of Sabaka *et al.* (2004) (blue curve) for $n < 40$. The difference w.r.t. the *MF4* model by Maus *et al.* (2005) is larger, despite of the fact that our model and *MF4* are derived from rather similar data sets, compared to *CM4* (which is based on data before 2002, and does not include CHAMP vector data). The discrepancy between our model and *MF4* is, therefore, possibly due to the different modelling approaches, for instance the serial track-by-track estimation of residual external fields used for *MF4* versus the co-estimation approach used here.

While a comparison of the power spectra of two models provides information on the magnitude of the respective magnetic fields, degree correlation, $\rho_n$, (Langel & Hinze 1998, eq. 4.23) yields information on the phase difference (and hence is independent of the power contained in a model). The right panel of Fig. 4 shows the degree correlation between the three models (the curves represent three-point moving averages). The degree correlation is near 0.95 between our model and *CM4* up to $n = 40$. Despite of the fact that similar data sets have been used for deriving *MF4* and our new model, the correlation with *MF4* yields a lower $\rho_n$ in this degree range. Beyond $n = 40$ the trend reverses and *CHAOS* compares more favourably with *MF4*.

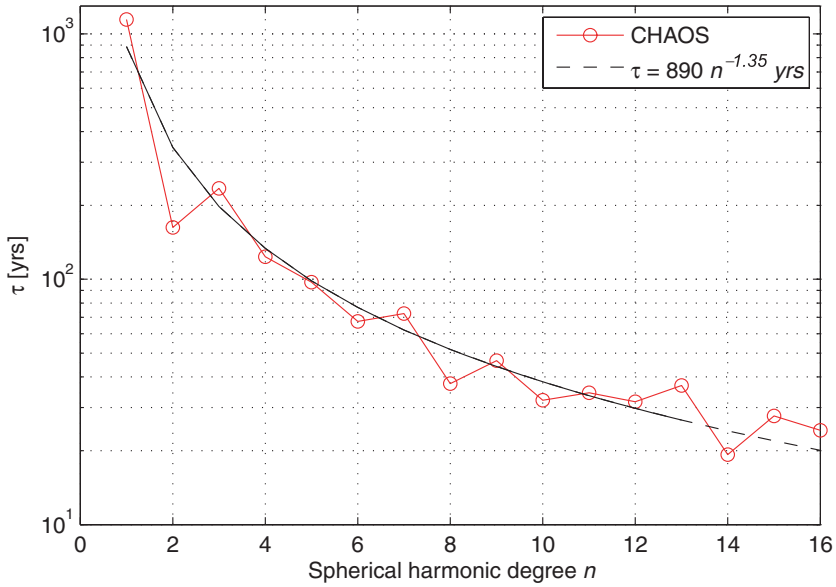


**Figure 3.** Dependence of core field reorganization time, $\tau$, on spherical harmonic degree $n$. Values derived from the presented model are shown as circles; the black line represents a power law fit.

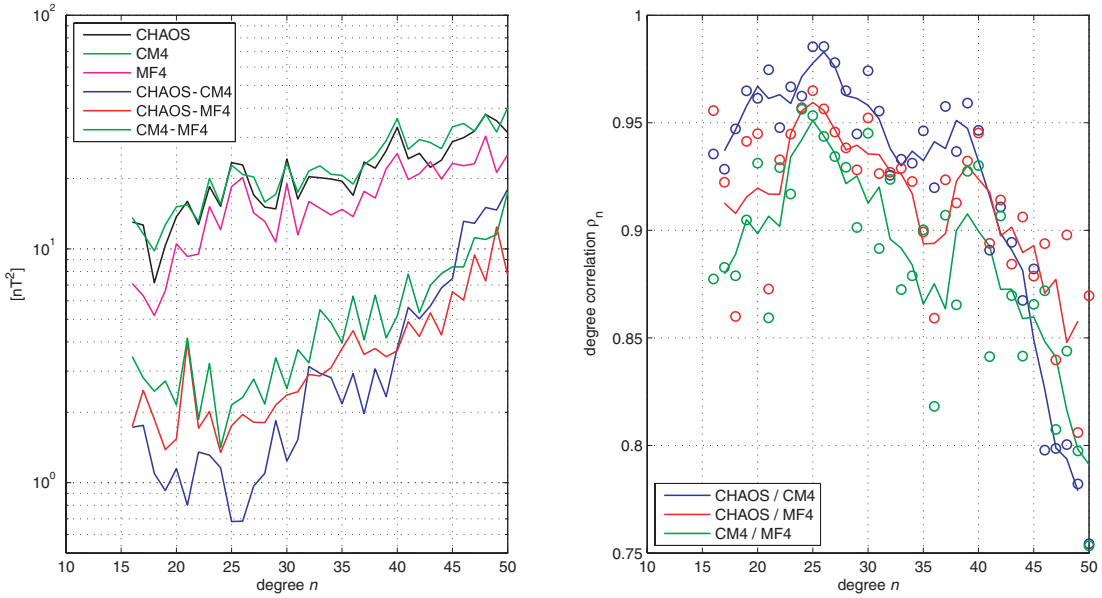


**Figure 4.** Left: Power spectra of the static field and of the field differences for various models. Right: Degree correlation.

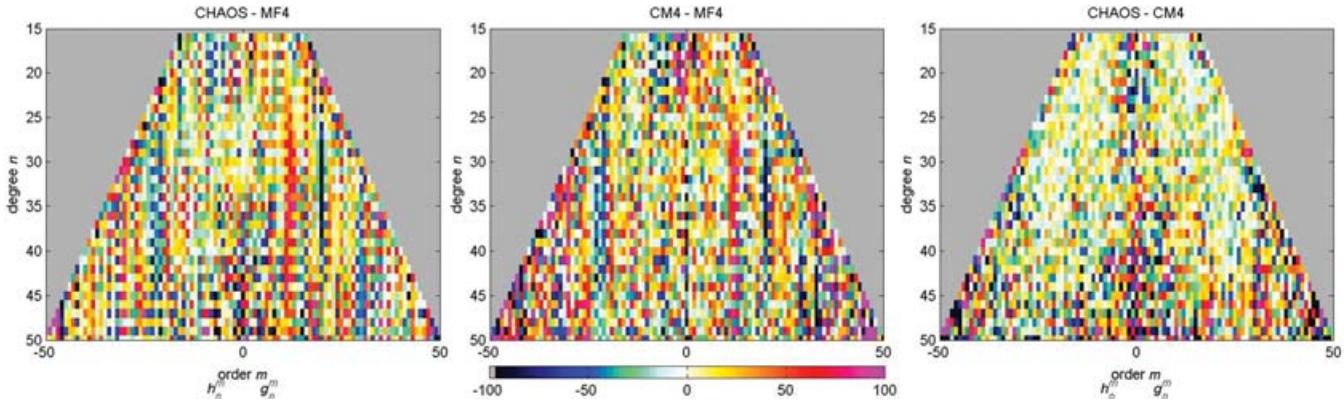


**Figure 5.** Sensitivity matrices (normalized coefficient differences in per cent) for various model pairs.

To further investigate the quality of the three models, sensitivity matrices are presented in Fig. 5. To obtain this quantity the difference between model coefficients is determined for all coefficients and subsequently normalized by the mean amplitude of the coefficients at degree $n$. In general, the figure confirms the better agreement between the new model and *CM4* (left panel) for $n \leq 40$, compared to *MF4*. There are, however, some discrepancies between our model and *CM4*, especially of the near-zonal terms, and of the near-sectorial terms for $n > 30$. However, the existence of some peculiar vertical stripes in the left and middle panel could indicate that coefficients of *MF4* with a certain order $m$ are biased, for example, $g_n^{12}$, $n = 25$–$45$, are significantly smaller than those of *CM4* and the new model, whereas $g_n^{20}$, $n = 25$–$45$, are significantly larger.

Maps of the radial magnetic field and field differences at 300 km altitude are shown in Fig. 6. They confirm the closer agreement between our model and *CM4*, compared to *MF4*. Both differences *CHAOS-MF4* (top right) and *CM4-MF4* (bottom left) contain north–south trending stripes and residuals of order of a few nT at middle latitudes. It is believed that these are caused by the orbit-by-orbit along-track filtering of the data used for *MF4*. Sabaka & Olsen (2006) demonstrated, using synthetic data, that a serial (as track-by-track) removal of large-scale magnetospheric fields (as done for *MF4*) may lead to a biased estimation of the underlying field. An unbiased estimate can be obtain by co-estimating these fields (the approach used in this paper).

While the difference between *CHAOS* and *MF4* is dominated by north–south aligned features (as is the difference between *CM4* and *MF4*), the differences *CM4-MF4* and *CM4-CHAOS* reveals a weak (about 2 nT at 300 km altitude) signal of the Equatorial Electrojet (*EEJ*). This probably indicates a leakage of the day-side *EEJ* signal into the *CM4*, which was derived using day- and night-side data. In addition, the difference *CM4-CHAOS* contains high-latitude features that are aligned with dipole latitudes and probably caused by contamination of either CM4 or CHAOS by the polar electrojets.

## 6 CONCLUSIONS

The presented CHAOS model results from a new modelling approach and includes almost 7 yr of data from the three magnetic missions currently in orbit, CHAMP, Ørsted and SAC-C. Our new modelling approach—taking into account the magnetometer vector data in the instrument frame, co-estimating the Euler angles to transform the magnetic data into the star imager frame, and

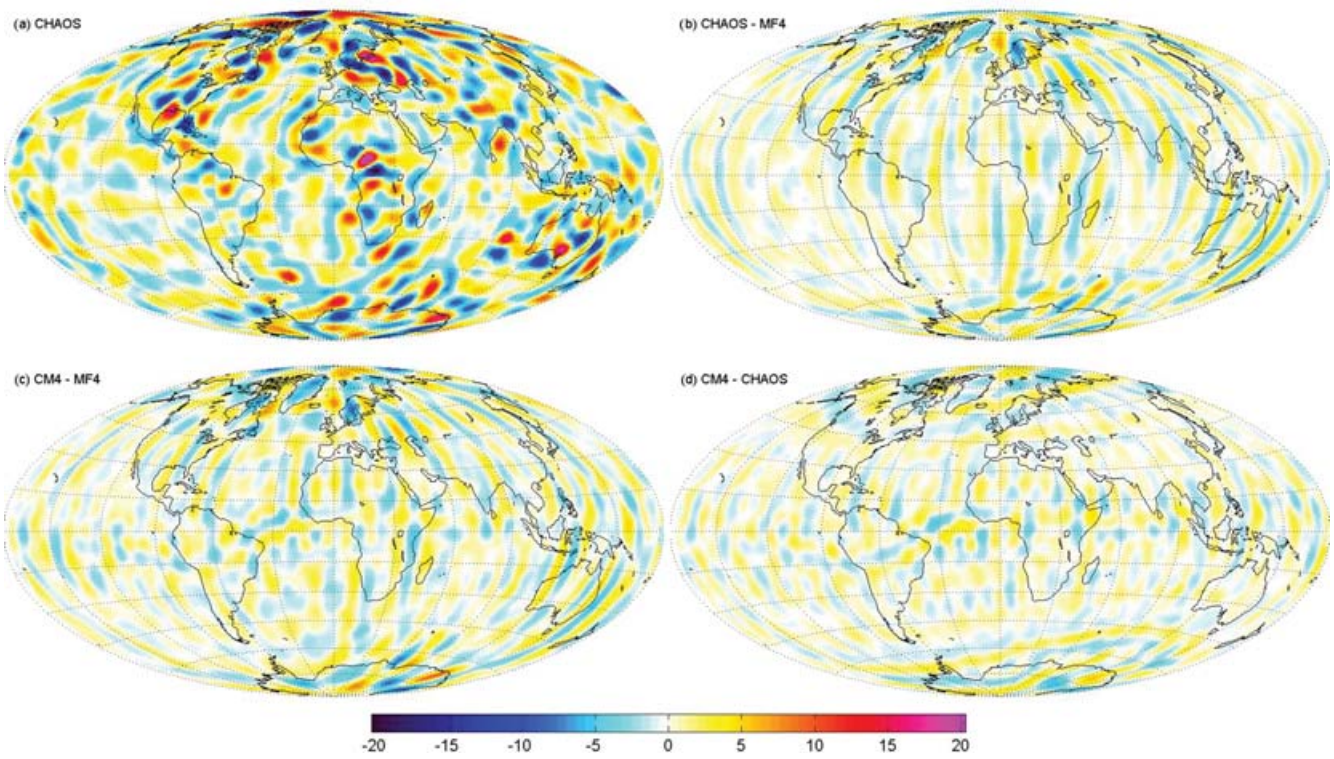


**Figure 6.** a: Map of the radial magnetic field (in nT) at 300 km altitude, calculated from coefficients of degrees $n = 16$–$40$. b–d: radial field differences for various model pairs.

considering the bending of the CHAMP optical bench—allows us to obtain a reliable description of the static part of the geomagnetic field up to at least degree $n = 40$, and of its first time derivative up to $n = 15$.

This new model brings two important improvements in describing the internal magnetic sources. First, the secular variation is no longer considered linear, as data covering more than 6.5 yr were used. A description of non-linear time changes was done by means of splines, to avoid unrealistic behaviours near the edges of the time interval. The new robust secular variation model allows us to evaluate a characteristic timescale for the core re-organization, which is of order 20 yr for structures with short wavelengths of about 1400 km at the core–mantle boundary. Secondly, the static field model, argued to be robust up to $n = 40$, is unbiased by different sources. Comparison with two other models (*MF4* and *CM4*) indicates that the *CHAOS* model is superior to previous model in the limits of its robustness. The model coefficients are available at www.spacecenter.dk/projects/oersted/models/ and at www.gfz-potsdam.de/pb2/pb23/Models/. Since the model was derived using observations taken between 1999 March and 2005 December, it is not recommended to extrapolate the spline coefficients describing the secular variation to time periods outside that interval.

The present study also demonstrates the possibilities of combining data from different satellite platforms. The new approach considered here is an important step in the preparation for the magnetic data provided by ESA's *Swarm* constellation mission (*cf.* www.esa.int/esaLP/LPswarm.html), scheduled for launch in 2010.

## ACKNOWLEDGMENTS

We would like to thank Cathy Constable, Nic Richmond and Alan Thomson for their constructive comments on an earlier version of the manuscript. The Ørsted Project was made possible by extensive support from the Danish Government, NASA, ESA, CNES and DARA. The operational support of the CHAMP mission by the German Aerospace Center (DLR) and the financial support for the data processing by the German Federal Ministry of Education and Research (BMBF) are gratefully acknowledged.

## REFERENCES

Bloxham, J. & Jackson, A., 1992. Time-dependent mapping of the magnetic field at the core-mantle boundary, *J. Geophys. Res.,* **97,** 19 537–19 563.

De Boor, C., 2001. A practical guide to splines, *Applied Mathematical Sciences,* **27**.

ESA, 1997. The Hipparcos and Tycho Catalogues, ESA SP-1200.

Feldstein, Y.I. & Starkov, G.V., 1970. The auroral oval and the boundary of closed field lines of geomagnetic field, *Planet. Space Science,* **18,** 501–508.

Holme, R., 2000. Modelling of attitude error in vector magnetic data: application to Ørsted data, *Earth, Planets and Space,* **52,** 1187–1197.

Holme, R. & Bloxham, J., 1996. The treatment of attitude errors in satellite geomagnetic data, *Phys. Earth Planet. Int.,* **98,** 221–233.

Holme, R. & Olsen, N., 2006. Core-surface flow modelling from high resolution secular variation, *Geoph. J. Int., in review*.

Holme, R., Olsen, N., Rother, M. & Lühr, H., 2003. CO2: A CHAMP magnetic field model, in *First CHAMP Mission results for Gravity, Magnetic and Atmospheric Studies*, eds Reigber, C., Lühr, H. & Schwintzer, P., p. 220–225, Springer Verlag, Berlin-Heidelberg-New York.

Hulot, G. & Le Mouël, J.L., 1994. A statistical approach to the Earth's main magnetic field, *Physics of the Earth and Planetary Interiors,* **82,** 167–183.

Kan, J.R. & Lee, L.C., 1979. Energy coupling function and solar wind-magnetosphere dynamo, *Geophys. Res. Lett.,* **6,** 577–580.

Kivelson, M.G. & Russell, C.T., 1995. *Introduction to Space Physics*, Cambridge University Press.

Langel, R.A. & Estes, R.H., 1985. The near-Earth magnetic field at 1980 determined from MAGSAT data, *J. Geophys. Res.,* **90,** 2495–2509.

Langel, R.A. & Hinze, W.J., 1998. *The Magnetic Field of the Earth's Lithosphere: The Satellite Perspective*, Cambridge University Press.

Langel, R.A., Ridgway, J.R., Sugiura, M. & Maezawa, K., 1988. The geomagnetic field at 1982 from DE-2 and other magnetic field data, *Journal of Geomagnetism and Geoelectricity,* **40,** 1103–1127.

Langlais, B., Mandea, M. & Ultré-Guérard, P., 2003. High-resolution magnetic field modeling: application to MAGSAT and Ørsted data, *Physics of the Earth and Planetary Interiors,* **135,** 77–91.

Lesur, V., Macmillan, S. & Thomson, A., 2005. A magnetic field model with daily variations of the magnetospheric field and its induced counterpart in 2001, *Geophys. J. Int.,* **160,** 79–88.

Lühr, H., Rother, M., Maus, S., Mai, W. & Cooke, D., 2003. The diamagnetic effect of the equatorial appleton anomaly: Its characteristics and impact on geomagnetic field modelling, *Geophys. Res. Lett.,* **30,** doi:10.1029/2003GL017407

Maus, S. & Lühr, H., 2005. Signature of the quiet-time magnetospheric magnetic field and its electromagnetic induction in the rotating Earth, *Geophys. J. Int.,* **162,** 755–763.

Maus, S. & Weidelt, P., 2004. Separating the magnetospheric disturbance magnetic field into external and transient internal contributions using a 1D conductivity model of the Earth, *Geophys. Res. Lett.,* **31,** L12,614, doi:10.1029/2004GL020, 232.

Maus, S., McLean, S., Dater, D., Lühr, H., Rother, M., Mai, W. & Choi, S., 2005. NGDC/GFZ candidate models for the 10th generation International Geomagnetic Reference Field, *Earth, Planets and Space,* **57,** 1151–1156.

Maus, S., Rother, M., Hemant, K., Stolle, C., Lühr, H., Kuvshinov, A.V. & Olsen, N., 2006. Earth's crustal magnetic field determined to spherical harmonic degree 90 from CHAMP satellite measurements, *Geophys. J. Int.*, doi:10.1111/j.1365-246X.2005.02833.x.

Olsen, N., 2002. A model of the geomagnetic field and its secular variation for epoch 2000 estimated from Ørsted data, *Geophys. J. Int.,* **149,** 454–462.

Olsen, N. et al., 2000. Ørsted initial field model, *Geophys. Res. Lett.,* **27,** 3607–3610.

Olsen, N. et al., 2003. Calibration of the Ørsted vector magnetometer, *Earth, Planets and Space,* **55,** 11–18.

Olsen, N., Sabaka, T.J. & Lowes, F., 2005. New parameterization of external and induced fields in geomagnetic field modeling, and a candidate model for IGRF 2005, *Earth, Planets and Space,* **57,** 1141–1149.

Ritter, P., Lühr, H., Maus, S. & Viljanen, A., 2004. High latiutude ionospheric currents during very quiet times: their characteristics and predictabilities, *Ann. Geophys.,* **22,** 2001–2014.

Sabaka, T.J. & Olsen, N., 2005. Enhancing comprehensive inversions using the *Swarm* constellation, *Earth, Planets and Space*, in press.

Sabaka, T.J., Olsen, N. & Purucker, M., 2004. Extending comprehensive models of the Earth's magnetic field with Ørsted and CHAMP data, *Geophys. J. Int.,* **159,** 521–547, doi: 10.1111/j.1365–246X.2004.02,421.x.

Schumaker, L.L., 1981. *Spline Functions: Basic Theory*, John Wiley & Sons, New York.

Seeber, G., 2004. *Satellite Geodesy*, Walter de Gruyter, Berlin—New York.

Stacey, F.D., 1992. *Physics of the Earth*, Brookfield Press, Kenmore, Australia.